Statistical Investigation of B-fields in Cores and Filaments using JCMT/SCUPOL Legacy Survey Archival Data

Porel P*

Indian Institute of Astrophysics, India

*Corresponding author: Puja Porel, Indian Institute of Astrophysics, Bengaluru, 560034, India, Email: puja.porel@iiap.res.in

Abstract

SCUPOL, the polarimeter for SCUBA on the James Clerk Maxwell Telescope was used for polarization observations of 104 regions at 850 μm wavelength and 15" resolution in the mapping mode by Matthews BC, et al. [1]. They presented the polarization values and magnetic field morphologies in these regions. In this work, we took the opportunity to use this big legacy survey data to investigate further the collective statistical properties of the measured polarization in different star-forming regions containing cores and filaments. We did not reproduce the polarization maps but used the polarization value catalogs to investigate the statistics of distributions. In some of these regions, the data from Combined Array for Research in Millimeter-wave Astronomy (CARMA) polarization observation at 1.3 mm wavelength and 2."5 resolution was also available from the TADPOL survey. We used that data and compared it with JCMT/SCUPOL values. We also study how the direction of outflows appears to relate the mean B-field direction from large scale (JCMT observation at 15") to small scale (CARMA observation 2.5") for the nine core regions common in both.

Keywords: ISM; Dust; Polarization; Magnetic Fields

Abbreviations

CARMA: Combined Array for Research in Millimeter-wave Astronomy; RAT: Radiative Alignment Torque; KDE: Kernal Density Estimation; AGB: Asymptotic Giant Branch; BG: Bok Globules, SC/PC: Starless or Prestellar Cores; SFR: Star-Forming Regions; YSO: Young Stellar Objects; VeLLOs: Very Low Luminosity Objects.

Introduction

Magnetic fields are crucial components in the star formation process, significantly influencing the dynamics involved [1-6]. The study of magnetic field morphology within the interstellar medium has been extensively advanced through observations of polarization caused by the alignment of interstellar dust grains. This phenomenon was initially discovered by Hall JS [7], and Hiltner WA [8,9]. For many years, the prevailing theory was that paramagnetic relaxation was responsible for aligning these rapidly rotating dust grains with the magnetic field. However, this alignment mechanism has faced significant challenges, both observationally and theoretically, revealing numerous limitations in its explanatory power [10,11].

The 'Radiative Alignment Torque' (RAT) theory is currently the most widely accepted mechanism for the alignment of interstellar dust grains. Initially proposed by Dolginov Z, et al. [12] and later fully developed by Draine T, et al. [13] and Lazarian A, et al. [11], this theory posits that in the presence of anisotropic radiation, the transfer of torques from photons to paramagnetic and non-spherical or

elongated dust grains induces a rapid spin-up of these grains. As a result of this rotation, the grains acquire a net magnetic moment through the Barnett effect, causing them to precess around the magnetic field. This magnetic moment further drives the angular momentum of the grains to precess around the magnetic field in a manner known as Larmor precession, ultimately aligning the grains' angular momentum parallel to the magnetic field lines. Over the past decade, numerous predictions of this theory have been substantiated, though the finer details of the mechanism and its components remain areas for further investigation [14].

When dust grains aligned by the interstellar magnetic field absorb radiation at shorter wavelengths, they re-emit this energy at longer wavelengths, specifically in the far infrared, millimeter, or sub-millimeter regions of the spectrum. The emitted radiation is polarized along the grains' long axis, meaning the electric field vector of the polarized emission is perpendicular to the plane-of-sky component of the local magnetic field.

Magnetic fields are typically well-ordered across large spatial scales, ranging from approximately 100 parsecs to 1 parsec [15]. However, on smaller, subparsec scales, magnetic fields can exhibit random orientations. This disarray is attributed to processes such as ambipolar diffusion and turbulent magnetic reconnection diffusion, which disrupt the coherence of the magnetic field lines [16-21].

In the paper, we used the JCMT/SCUPOL data from legacy surveys in some cores and filaments and the TADPOL archival data in some regions which are common in both studies. We used the available polarization measurements to infer: mean B-field orientations, the statistical distribution of polarization values, relations between large (JCMT at 15" resolution) and small (CARMA at 2.5" resolution) scale B-fields, and the relation between outflow orientations with mean B-field orientations at different spatial scales. This work uses the opportunity to do statistical analysis of the available polarization measurements which was not presented in the original paper of JCMT/SCUPOL legacy survey [1]. Here section 2 presents data acquisition details, section 3 shows the results of our analysis, and section 4 summarises this study.

Methodology

The JCMT-SCUPOL data

In this study, we utilized SCUPOL data to explore the statistical properties of magnetic fields within core and filamentary structures. This dataset, derived from the comprehensive work The Legacy of SCUPOL: 850 μm Imaging Polarimetry from 1997 to 2005, encompasses polarimetric observations performed by SCUPOL, the polarimeter for SCUBA on the James Clerk Maxwell Telescope (JCMT), covering the period from 1997 to July 2005 [1]. While SCUBA facilitated simultaneous observations at both 850 μm and 450 μm, the 450 μm data were either unavailable or had insufficient sensitivity for the regions analyzed. As a result, our study is exclusively based on 850 μm observations, targeting various astrophysical environments, including cores, filaments, ridges, galaxies, planetary nebulae, asymptotic giant branch (AGB) stars, and supernova remnants, with a particular emphasis on cores and filaments. Within core regions, we focused on four primary categories: Bok globules (BG), starless or prestellar cores (SC/PC), star-forming regions (SFR), and young stellar objects (YSO). Data reduction and processing were accomplished using the Starlink software suite, including the SURF, KAPPA, POLPACK, and CURSA packages, yielding an angular resolution of 15" and the detailed data reduction procedure is described in Matthews BC, et al. [1]. Further, we supplemented our analysis with data from additional specific cores of interest.

The CARMA Data

To examine the dynamic interplay between outflows from core regions and magnetic fields across different spatial scales, we incorporated data from the TADPOL survey, as detailed in the publication TADPOL: A 1.3 mm Survey of Dust Polarization in Star-Forming Cores and Regions [2]. This survey presents 1.3 mm polarimetric observations from the Combined Array for Research in Millimeter-wave Astronomy (CARMA), encompassing dust polarization data for 30 star-forming cores and 8 star-forming regions. The TADPOL data provide high-resolution magnetic field maps on a more localized scale, with a spatial resolution of 2.5", offering a finer level of detail than the JCMT/SCUPOL observations, thereby enhancing our ability to probe magnetic field structure on smaller scales. The data reduction methodology for the CARMA observations is thoroughly described in Hull CLH, et al. [2].

Results

Statistical Analysis of the Core Polarization Data

Magnetic Fields in the Cores: To examine the morphology of magnetic fields within core regions, we selected a subset of 45 cores from the dataset presented by Matthews BC, et al. [1], which involved dust polarization observations conducted at a wavelength of 850 μm using the JCMT/SCUPOL system, achieving a resolution of 15". In this study, data were sampled at an angular resolution of 10" with select regions binned to 20", as elaborated in Matthews BC, et al. [1] and included only areas exhibiting significant polarization vectors. The selected regions meet the stringent criteria of $p/dp > 2$, $dp < 4\%$, and I

Porel P. Statistical Investigation of B-fields in Cores and Filaments using JCMT/SCUPOL Legacy Survey Archival Data. Open J of Astro 2024, 2(2): 000144.

Copyright© Porel P.

> 0, where I represents the Stokes intensity parameter and p denotes the polarization degree.

To investigate the variation in outflow direction in relation to the mean magnetic field direction across different scales, we further narrowed our focus to nine core regions shared between the 30 star-forming cores and 8 star-forming regions observed in the Combined Array for Research in Millimeter-wave Astronomy (CARMA) at a wavelength of 1.3 mm with a resolution of 2.5" [2]. These nine core regions are common to both the CARMA and JCMT observations, allowing for a comparative analysis of magnetic field dynamics in these astrophysical environments.

Histogram of θ_B and Scatter Plot of p vs. θ_B: In the JCMT/SCUPOL dataset, the position angles (θ_E) of the polarization E-vector at a wavelength of 850 μm are provided. To derive the position angle (θ_B) of the B-vector, θ_E is rotated by 90°, after which a histogram is constructed to illustrate the distribution of θ_B for each individual core region. The blue dotted line in these histograms represents the mean position angle of the magnetic fields (θ_{Bmean}) across the respective core regions.

Additionally, the scatter plot depicting the degree of polarization (p) against the B-vector position angle (θ_B) reveals the relationship between polarization and magnetic field orientation. Figure 1 displays the histogram of θ_B alongside the scatter plot of p versus θ_B for selected cores. The error bars in the scatter plots indicate the uncertainties associated with each p and θ_B measurement.
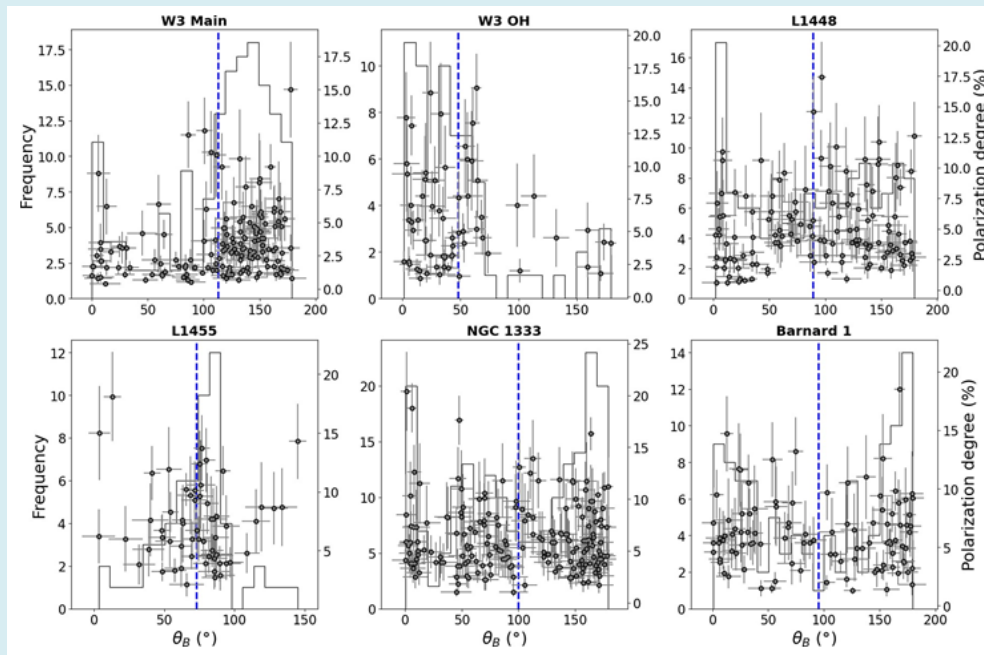

Figure 1: Histogram of θ_B and scatter plot of polarization degree (p) vs. θ_B with error bars for the core regions. The histograms illustrate the distribution of magnetic field vector position angles (θ_B), with a blue dotted line in each plot indicating the mean position angle (θ_{Bmean}) for the respective core regions. The scatter plots depict the polarization degree (p) across various position angles in these regions, with error bars representing the uncertainties associated with each value of p and θ_B.

The scatter plots, inclusive of error bars, reveal that the majority of data points cluster within the ranges of 113° < θ_B < 175° and 0.8% < p < 6% for the W3 Main region, as well as within 0° < θ_B < 75° and 1% < p < 16% for the W3 OH region. In contrast, the remaining plots exhibit a greater dispersion in both p and θ_B values, indicating a more complex relationship in those regions.

Histogram and Kernal Density Estimation (KDE) of the difference between θ_{minor} and θ_{Bmean}: The angle (θ_{minor}) formed by the minor axis of an ellipse, which is roughly fitted to the core region, with respect to the vertical line (the north-south direction) is measured in an anticlockwise manner. This ellipse is approximated either inside or outside the outermost contour of the core region, as delineated in Matthews BC, et al. [1]. The B-vector position angles (θ_B) for individual cores are derived by adding 90° to the θ_E values provided in the SCUPOL dataset. Subsequently, the mean B-vector position angle (θ_{Bmean}) is computed for each core. Figure 2 illustrates the measurement procedure for θ_{minor}, θ_{Bmean}, and Δθ with respect to the reference direction (northsouth).

Porel P. Statistical Investigation of B-fields in Cores and Filaments using JCMT/SCUPOL Legacy Survey Archival Data. Open J of Astro 2024, 2(2): 000144.
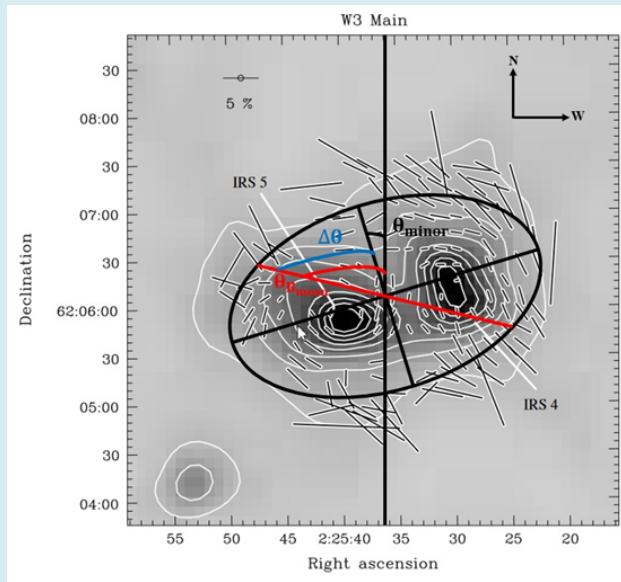
Copyright© Porel P.

Figure 2: Measurement of the minor axis angle (θ_{minor}), the mean magnetic field angle (θ_{Bmean}), and the angular difference between these orientations ($\Delta\theta$) for the W3 Main region. The color map is adapted from Matthews BC, et al. [1], as the polarization map was not re-created in this study.

Name	RA (J2000)	DEC (J2000)	Object type	θ_{minor} (°)	θ_{Bmean} (°)	$\Delta\theta$(°)	Distance (kpc)
W3 Main	02 25 35.44	+62 06 16.4	SFR (HM)	17	113 ± 9	96 ± 9	1.95 [19]
W3 OH	02 27 03.83	+61 52 24.8	SFR (HM)	141	48 ± 9	93 ± 9	1.95 [19]
L1448	03 25 38.80	+30 44 05.4	YSO (Class 0)	80	89 ± 10	9 ± 10	0.250 ± 0.050 [20]
L1455	03 27 41.31	+30 12 39.4	SFR (LM)	45	73 ± 9	28 ± 9	0.250 ± 0.050 [20]
NGC 1333	03 29 11.11	+31 13 20.2	SFR (HM)	89	100 ± 9	11 ± 9	0.320 [21]
Barnard 1	03 33 17.88	+31 09 32.9	SFR (LM)	99	95 ± 9	4 ± 9	0.250 ± 0.050 [20]
HH211/IC348	03 43 56.70	+32 00 51.9	SFR (LM)	120	114 ± 6	6 ± 6	0.250 ± 0.050 [20]
L1498	04 10 52.60	+25 10 00.0	SC/PC	36	123 ± 9	87 ± 9	0.14 ± 0.02 [22]
L1527	04 39 53.90	+26 03 10.0	YSO (Class 0)	35	75 ± 9	40 ± 9	0.140 ± 0.010 [23]
IRAM 04191+1522	04 21 56.91	+15 29 46.1	YSO (Class 0)	164	64 ± 8	100 ± 8	0.140 ± 0.010 [23]
L1544	05 04 17.23	+25 10 43.7	SC/PC	55	61 ± 10	6 ± 10	0.140 ± 0.010 [23]
NGC 2071 IR	05 47 04.85	+00 21 47.1	SFR (HM)	80	89 ± 10	9 ± 10	0.400 [24]
IRAS 05490+2658	05 52 13.24	+26 59 33.3	SFR (HM)	77	71 ± 10	6 ± 10	2.1 [25]
Mon R2 IRS	06 07 46.16	-06 23 22.5	SFR (HM)	110	51 ± 8	59 ± 8	0.950 [26]
MON IRAS 12	06 41 05.81	+09 34 09.0	SFR (HM)	115	67 ± 5	48 ± 5	0.800 [27]
CB 54	07 04 21.07	-16 23 20.09	BG	70	78 ± 10	8 ± 10	1.1 [28]
L183	15 54 08.96	-02 52 43.9	SC/PC	80	86 ± 9	6 ± 9	0.15 [29]
ρ Oph A	16 26 26.45	-24 24 10.9	SFR (IM)	96	103 ± 8	7 ± 8	0.139 [30]
ρ Oph C	16 27 00.10	-24 34 26.7	SFR (IM)	25	88 ± 9	63 ± 9	0.139 [30]
ρ Oph B2	16 27 27.97	-24 27 06.8	SFR (IM)	170	93 ± 9	77 ± 9	0.139 [30]
L43	16 34 35.57	-15 47 00.6	SC/PC	39	101 ± 9	62 ± 9	0.17 [29]
NGC 6334A	17 20 19.55	-35 54 42.3	SFR (HM)	158	97 ± 10	61 ± 10	1.7 [31]

Porel P. Statistical Investigation of B-fields in Cores and Filaments using JCMT/SCUPOL Legacy Survey Archival Data. Open J of Astro 2024, 2(2): 000144.

Copyright© Porel P.

GGD 27	18 19 12.00	-20 47 30.9	SFR (HM)	117	74 ± 10	43 ± 10	1.7 [32]
CRL 2136 IRS 1	18 22 26.48	-13 30 15.1	SFR (HM)	100	106 ± 10	6 ± 10	2 [33]
Serpens Main Core	18 29 49.34	+01 15 54.6	SFR (LM)	65	97 ± 8	32 ± 8	0.310 [34]
CL 04/CL 21	18 37 19.39	-07 11 31.8	SFR (HM)	108	119 ± 9	11 ± 9	0.770 [35]
G28.34+0.06	18 42 52.40	-03 59 53.9	SFR (HM)	89	104 ± 10	15 ± 10	4.8 [36]
IRAS 18437-0216	18 46 23.23	-02 13 45.4	SFR (HM)	84	77 ± 9	7 ± 9	6.6 [37]
W48	19 01 45.45	+01 13 04.5	SFR (HM)	10	76 ± 8	66 ± 8	3.4 [38]
R Cr A	19 01 53.65	-36 57 07.5	SFR (HM)	99	100 ± 10	1 ± 10	0.130 [39]
W49	19 10 13.60	+09 06 17.4	SFR (HM)	100	100 ± 6	0 ± 6	11.4 [40]
W51	19 23 42.00	+14 30 33.0	SFR (HM)	90	98 ± 9	8 ± 9	7.5 [41]
IRAS 20081+2720	20 10 13.99	+27 28 36.9	SFR (LM)	14	29 ± 9	15 ± 9	0.700 [42]
AFGL 2591 IRS	20 29 24.72	+40 11 18.9	SFR (HM)	150	114 ± 9	36 ± 9	1.5 [43]
IRAS 20188+3928	20 20 38.75	+39 38 03.9	SFR (HM)	98	110 ± 9	12 ± 9	0.4 – 4 [44]
S106	20 27 17.32	+37 22 41.3	SFR (HM)	155	96 ± 8	59 ± 8	0.600 [45]
G079.3+0.3	20 32 23.62	+40 19 44.0	SFR (LM)	117	130 ± 9	13 ± 9	1 [36]
S140	22 19 18.00	+63 18 49.0	SFR (HM)	92	87 ± 8	5 ± 8	0.900 [46]
S146	22 49 28.56	+59 55 08.6	SFR (HM)	89	89 ± 9	0 ± 9	5.2 [47]
Cepheus A	22 56 17.80	+62 01 49.0	YSO (Class 0/I)	147	71 ± 8	76 ± 8	0.730 [48]
S152	22 58 50.14	+58 45 01.0	SFR (HM)	71	122 ± 9	51 ± 9	5 [49]
NGC 7538	23 13 45.54	+61 27 35.7	SFR (HM)	90	113 ± 8	23 ± 8	2.8 [50]
S157	23 16 04.00	+60 02 06.0	SFR (HM)	64	79 ± 10	15 ± 10	2.5 [51]

Table 1: Table for calculating $\Delta\theta$ (= $|\theta_{Bmean} - \theta_{minor}|$).

The analysis summarized in Table 1 reveals a striking alignment in certain cores, notably W49 and S146, where the $\Delta\theta$ value approaches $0°$, defined as $\Delta\theta = \theta_{Bmean}$ θ_{minor}. This close alignment signifies that the mean magnetic field in these cores is precisely oriented along the minor axis. In contrast, this parallelism is less pronounced or absent in other cores.
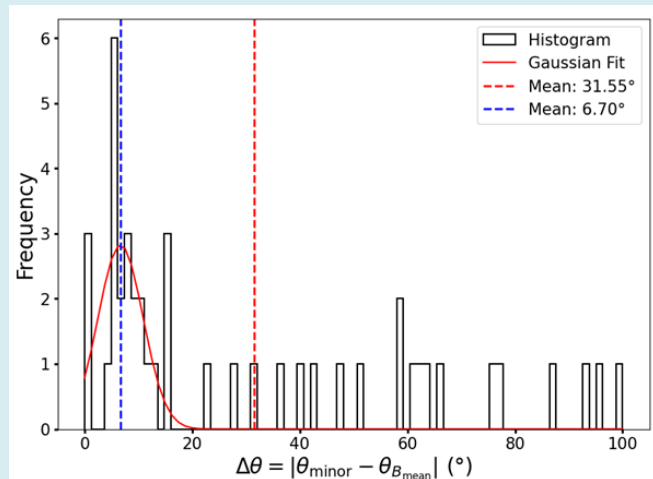

Figure 3: Histogram of the angular difference, $\Delta\theta$ (θ_{Bmean} θ_{minor}), for the core regions. This histogram illustrates the distribution of $\Delta\theta$ values computed for the cores identified in Table 1, with a red curve superimposed to depict the Gaussian fit to the data. The vertical dashed lines, colored red and blue, represent the mean value of $\Delta\theta$ and the peak of the fitted Gaussian curve, respectively, providing insight into the central tendency and most probable value of the angular difference.
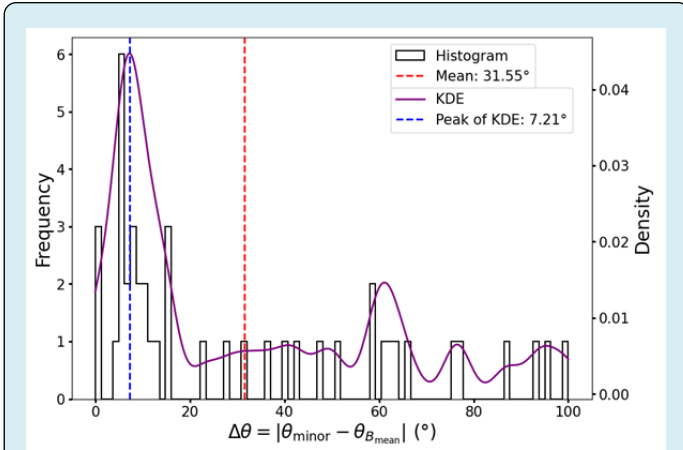
Porel P. Statistical Investigation of B-fields in Cores and Filaments using JCMT/SCUPOL Legacy Survey Archival Data. Open J of Astro 2024, 2(2): 000144.

Copyright© Porel P.

Figure 4: KDE plot (depicted by the purple curve) of the angular difference, $\Delta\theta = (\theta_{Bmean} - \theta_{minor})$, for the core regions, overlaid on the histogram of $\Delta\theta$ values derived from the cores listed in Table 1. The red and blue dashed lines indicate the mean value of $\Delta\theta$ and the peak of the KDE curve, respectively, highlighting the central tendency and the most probable value of the angular difference within the data distribution.

To illustrate the distribution of $\Delta\theta$, we generated a histogram, displayed in Figure 3, with a red curve representing a Gaussian fit. This fit peaks at approximately 6.70°, indicating a prevalent trend in $\Delta\theta$ alignment. Figure 4 presents the Kernel Density Estimate (KDE) plot of the $\Delta\theta$ histogram, peaking at around 7.21°, reinforcing the observed alignment trend. Both the Gaussian fit and KDE plot peaks suggest that the majority of cores exhibit a minor axis orientation closely aligned with the mean magnetic field direction.

From Table 1, we calculate the mean $\Delta\theta$ value as 32° $\pm$ 9°. This average supports the notion that the magnetic field direction within these core regions predominantly aligns with the minor axis. Such an orientation is consistent with observations by SCUPOL, highlighting a significant degree of parallelism between the magnetic field and structural morphology within these astrophysical cores. Additionally, Soam A, et al. [52] showed that the mean magnetic field direction with the minor axes of a limited sample of five cores is approximately 37°, further implying that the mean B-field is nearly parallel to the minor axis of these core regions.

The dispersion of $\Delta\theta$ values within the core regions is approximately 30.19°. This substantial dispersion indicates that the B-field position angles exhibit a random alignment in the JCMT-SCUPOL observations.

Overall, this study provides a statistical representation of the magnetic field morphology in the plane of the sky,

consistent with previous hypotheses.

Difference between Outflow and Mean B-field Orientation: In the TADPOL survey, a detailed examination of dust polarization was conducted using observations from the Combined Array for Research in Millimeter-wave Astronomy (CARMA) at a wavelength of 1.3 mm, targeting 30 star-forming cores and 8 star-forming regions. Through these observations, the small-scale magnetic field orientation (χ_{sm}) was determined with a resolution of 2″.5 within the identified core regions. Additionally, the angle of the outflow ejection (χ_0) was also calculated [2].

Prior to section 3.1.4, the mean magnetic field position angle (θ_{Bmean}) for each individual core region was derived from JCMT/SCUPOL data. Notably, θ_{Bmean} represents the mean value of the B-vector position angle on a large scale, which is significantly larger than the scale of the CARMA observations.

All angles—χ_{sm}, χ_0, and θ_{Bmean} —are measured in an anticlockwise direction with respect to the north-south orientation.

Between the CARMA and JCMT surveys, we identified nine common core regions that facilitated a comparative analysis of the variation in outflow direction between large-scale and small-scale magnetic fields, which we visualized using a Kernel Density Estimate (KDE) plot.
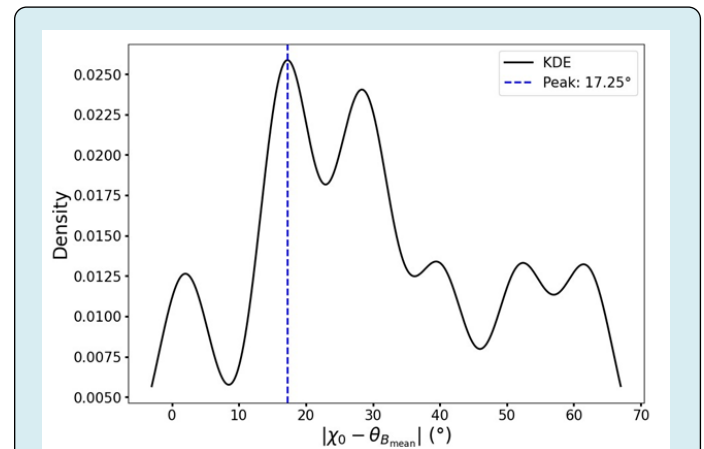

Figure 5: KDE plot depicting the angular difference between θ_{Bmean} and χ_0 for the nine cores observed in both JCMT and CARMA datasets. The blue dashed line marks the peak of the KDE curve for $\theta_{Bmean}-\chi_0$, which occurs at 17.25 °. This value suggests that, on a large scale, the outflow direction for these cores is nearly aligned with the mean magnetic field orientation.

The KDE plot depicting the angular difference between θ_{Bmean} and χ_0 is shown in Figure 5. In this plot, the blue dashed

line highlights a peak value of θ_{Bmean} χ_0 around 17.25°, while the mean value, calculated from Table 2, is approximately 31° 8°. These findings collectively suggest that the outflow emanating from the core regions aligns closely with the mean magnetic field direction on large scales. In a study by Soam

A, et al. [52], an examination of five cores containing Very Low Luminosity Objects (VeLLOs) showed that the outflows in three of these cores exhibit a significant tendency to align with the magnetic field orientation within the surrounding envelope.
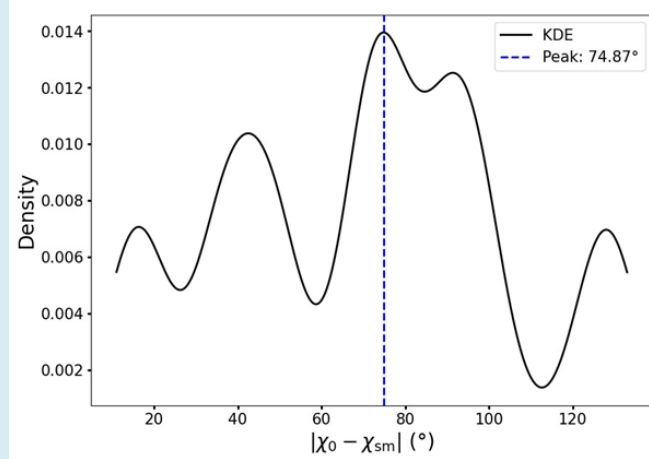

Figure 6: KDE plot depicting the angular difference between χ_{sm} and χ_0 for the nine cores observed in both JCMT and CARMA datasets. The blue dashed line marks the peak of the KDE curve for χ_0 χ_{sm}, which occurs at 74.87 °. This value suggests that, on a small scale, the outflow direction for these cores is nearly perpendicular to the mean magnetic field orientation.

Following this, we present the KDE plot for the angular difference between χ_0 and χ_{sm} in Figure 6. Here, the blue dashed line indicates a peak value of χ_{sm} - χ_0 at 74.87°, while the mean value, derived from Table 2, is approximately 70° ± 36°. These results imply that, at smaller scales, the outflow direction within the core regions is predominantly

orthogonal to the mean magnetic field orientation. This finding is consistent with Hull CLH, et al. [2], who observed that, on smaller scales, the outflow direction tends to be nearly perpendicular to the mean magnetic field position angle.

No.	Name	p (%)	χ_{sm} (°)	χ_0 (°)	θ_{Bmean} (°)	$\|\theta_{Bmean} - \chi_0\|$ (°)	$\|\chi sm - \chi_0\|$ (°)
1	L1448C	5 ± 2	26 ± 37	97	89 ± 10	40 ± 10	71 ± 35
	L1448N	5 ± 2	112 ± 32	161	89 ± 10	40 ± 10	71 ± 35
2	NGC 1333- IRAS 2Ac	6 ± 2	70 ± 23	59.5	100 ± 9	62 ± 9	16 ± 25
	SVS 13	6 ± 2	6 ± 24	...	100 ± 9	62 ± 9	16 ± 25
	NGC 1333- IRAS 4A	6 ± 2	56 ± 20	18	100 ± 9	62 ± 9	16 ± 25
	NGC 1333- IRAS 4B	6 ± 2	84 ± 34	0	100 ± 9	62 ± 9	16 ± 25
	NGC 1333- IRAS-4B2	6 ± 2	55 ± 20	76	100 ± 9	62 ± 9	16 ± 25
3	HH211MM	9 ± 2	164 ± 32	116	114 ± 6	2 ± 6	48 ± 32
4	L1527	7 ± 2	3 ± 8	92	75 ± 9	17 ± 9	89 ± 8
5	CB 54	6 ± 2	32 ± 42	108	78 ± 10	30 ± 10	76 ± 42
6	VLA 1623	5 ± 1	23 ± 48	120	103 ± 8	17 ± 8	97 ± 48
7	Ser-emb 8	7 ± 2	7 ± 44	123	97 ± 8	27 ± 8	37 ± 33
	Ser-emb 8(N)	7 ± 2	83 ± 15	107	97 ± 8	27 ± 8	37 ± 33
	Ser-emb 6	7 ± 2	172 ± 33	135	97 ± 8	27 ± 8	37 ± 33
8	NGC 7538	4 ± 1	52 ± 62	...	113 ± 8	...	...
9	CB 244	12 ± 3	170 ± 49	42	94 ± 7	52 ± 7	128 ± 49

Table 2: Table for observational values of small-scale magnetic field χsm and outflow direction χ0 for core regions.

Porel P. Statistical Investigation of B-fields in Cores and Filaments using JCMT/SCUPOL Legacy Survey Archival Data. Open J of Astro 2024, 2(2): 000144.

Copyright© Porel P.

Table 2 consolidates the computed values of θ_{Bmean} χ_0 and χ_{sm} - χ_0 across the nine cores examined, providing a clear summary of the observed alignment trends at both large and small scales.

Kernel Density Estimation plot of χ_{sm} (CARMA data) and θ_{Bmean} (JCMT data): This study demonstrated that the alignment between the large-scale and small-scale magnetic fields in core regions was not entirely parallel, as illustrated in Figure 7. The smallscale observations, which provided a magnified view of the larger scales, revealed a more intricate structure of the magnetic field orientation deep within the cores. This observed misalignment between the largescale and small-scale magnetic field directions contributed to a low degree of polarization (p). This phenomenon suggested that the alignment of dust grains was disrupted by the random orientations of magnetic fields at smaller scales [2]. The transition from large to small spatial scales unveiled a significantly more complex polarization pattern, characterized by distorted magnetic field geometries. Furthermore, evidence of hourglass morphologies was apparent in the densest regions of some cores, indicating the intricate interplay between the magnetic fields and the surrounding matter.
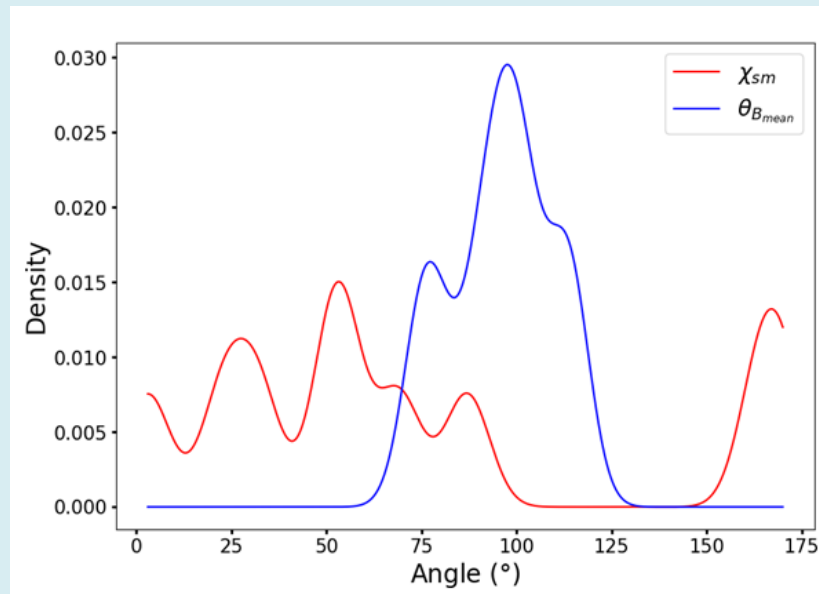

Figure 7: KDE plot of χ_{sm} and θ_{Bmean} for nine cores common in CARMA and JCMT observations which clearly shows the misalignment of large and small scale mean magnetic field direction in those nine core regions.

Statistical analysis of the Filament Polarization Data

In this section, the magnetic field morphology in the filament regions is studied in detail.

Magnetic Field in Filament Regions: In this study, the data were sampled at a resolution of 10"; in certain instances, it was binned to 20", as detailed in Matthews BC, et al. [1]. The dataset exclusively comprises regions where significant polarization vectors were detected, adhering to the criteria of p/Δp > 2, Δp < 4%, and I > 0. To investigate the morphology of magnetic fields within filament regions, we selected six filaments that were observed using the JCMT/SCUPOL at a wavelength of 850 μm and a resolution of 15" [1].

Histogram of θ_B and scatter plot of p vs. θ_B and KDE plot of the difference between θ_{major} and θ_{Bmean}: The histogram illustrating the position angle (θ_B) of the B-vector, along with the scatter plot depicting the degree of polarization (p) against θ_B (Figure 8), was constructed following the methodology employed for the core regions. These histograms reveal the distribution of θ_B, with the blue dotted line indicating the mean value of the magnetic field position angle, denoted as θ_{Bmean}. The scatter plot presents the degree of polarization at varying angles θ_B, with error bars representing the uncertainties associated with the corresponding p and θ_B values.
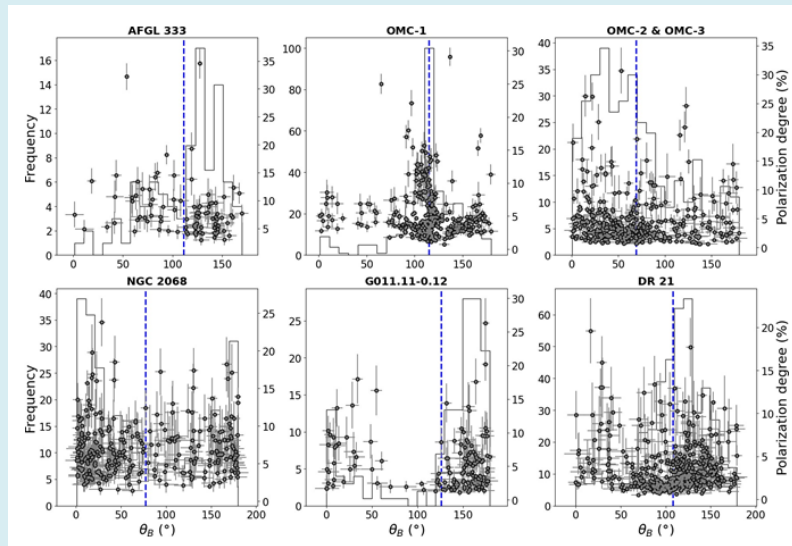
Porel P. Statistical Investigation of B-fields in Cores and Filaments using JCMT/SCUPOL Legacy Survey Archival Data. Open J of Astro 2024, 2(2): 000144.

Copyright© Porel P.

Figure 8: Histogram of θ_B and scatter plot of p vs. θ_B with the error bars for the filament regions. The histograms show the distribution of B-vector position angles (θ_B) and the blue dotted line in each of the histograms shows the mean value of B-vector position angle (θ_{Bmean}) in those individual filament regions. The scatter plots show the polarization degree (p) at different position angles for those filament regions and the error bars are the uncertainties in each p and θ_B value.

The scatter plots, inclusive of error bars, demonstrate that the majority of data points are confined within the following ranges: $113° < \theta_B < 160°$ and $3\% < p < 10\%$ for the AFGL 333 region; $90° < \theta_B < 130°$ and $1\% < p < 16\%$ for the OMC-1 region; $0° < \theta_B < 100°$ and $0.8\% < p < 8\%$ for the OMC-2 & OMC-3 regions; $125° < \theta_B < 177°$ and $1\% < p < 10\%$ for the G011.11-0.12 region; and $75° < \theta_B < 175°$ and $0.6\% < p <$ 7% for the DR 21 region. The angle θ_{major}, defined as the angle between the major axis of the filament and the reference north-south direction, represents the longest dimension of the filament, which is delineated within the outermost contour of the respective region, as described in Matthews BC, et al. [1]. Figure 9 illustrates how the θ_{major} and θ_{Bmean} are measured for the filament AFGL 333.
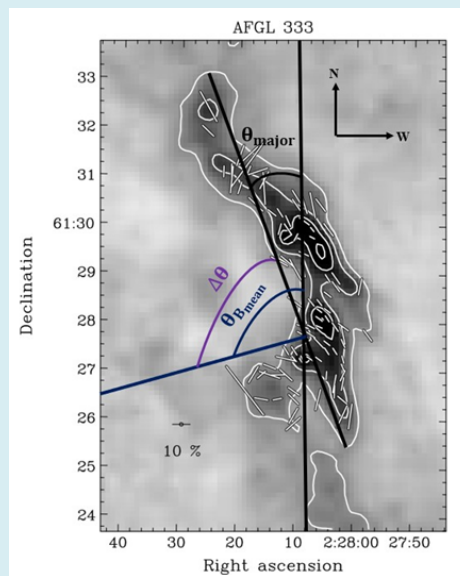

Figure 9: Measurement of the minor axis angle (θ_{major}), the mean magnetic field angle (θ_{Bmean}), and the angular difference between these orientations ($\Delta\theta$) for AFGL 333 region. The color map is adapted from Matthews BC, et al. [1], as the polarization map was not re-created in this study.

Porel P. Statistical Investigation of B-fields in Cores and Filaments using JCMT/SCUPOL Legacy Survey Archival Data. Open J of Astro 2024, 2(2): 000144.

Copyright© Porel P.

Name	RA (J2000)	DEC (J2000)	Object type	θ_{major} (°)	θ_{Bmean} (°)	$\Delta\theta$(°)	Distance (kpc)
AFGL 333	02 28 08.81	+61 29 25.0	SFR (HM)	19	111 ± 7	92 ± 7	1.95 [19]
OMC-1	05 35 14.5	-05 22 33.0	SFR (HM)	10	115 ± 4	105 ± 4	0.414 ± 0.007 [53]
OMC-2 & OMC-3	05 35 26.9	-05 09 58	SFR (LM)	166	69 ± 7	97 ± 7	0.414 ± 0.007 [53]
NGC 2068	05 46 37.64	+00 00 33.1	SFR (LM)	62	77 ± 8	15 ± 8	0.400 [24]
G011.11-0.12	18 10 33.99	-19 21 36.9	SFR (HM)	55	126 ± 8	71 ± 8	3.6 [36]
DR 21	20 39 01.50	+42 19 38.0	SFR (HM)	176	108 ± 9	68 ± 9	3 [54]

Table 3: Table to calculate $\Delta\theta = |\theta_{major} - \theta_{Bmean}|$ for individual filament region.

The mean value of $\Delta\theta$ (defined as θ_{Bmean} θ_{major}), indicating the deviation of the mean B-field direction from the major axis of the filament, is computed to be 75° 7° as derived from Table 3. This finding suggests that the major axis of the filament is nearly perpendicular to the direction of the mean magnetic field.

This observation is further corroborated by the KDE plot (Figure 10), which illustrates the peak value of the KDE of ($\Delta\theta$) mean at 70°, indicated by the blue dashed line.
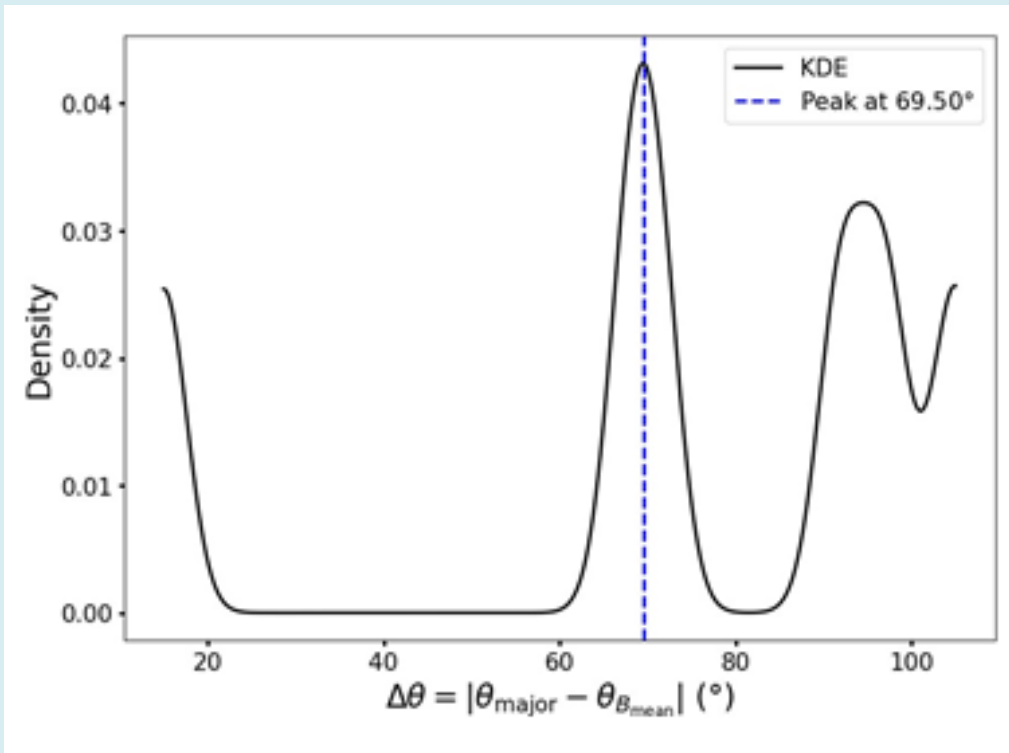

Figure 10: KDE plot of the angular difference, $\Delta\theta$ (= θ_{Bmean} θ_{major}), for the filament regions. The blue dashed line denotes the peak of the KDE curve for $\Delta\theta$, which occurs at 69.50°. This suggests that the plane-of-sky component of the mean magnetic field is nearly perpendicular to the major axis of the filamentary structures.

The dispersion of $\Delta\theta$ values within the filament regions is approximately 29.83°. This substantial dispersion highlights the random alignment of the B-field position angles within these filamentous structures.

Histogram of the difference between θ_{major} and θ_{Bi}: The histogram depicting the difference between θ_{major} and θ_{Bi} (Figure 11) elucidates the extent to which the observed position angle of the magnetic field, θ_{Bi}, deviates from the major axis of each filament region.

For all filament regions analyzed, the observed differences between θ_{major} and θ_{Bi} indicate a predominant trend where the major axis of the filament is nearly perpendicular to the corresponding observed position angle of the magnetic field (θ_{Bi}).
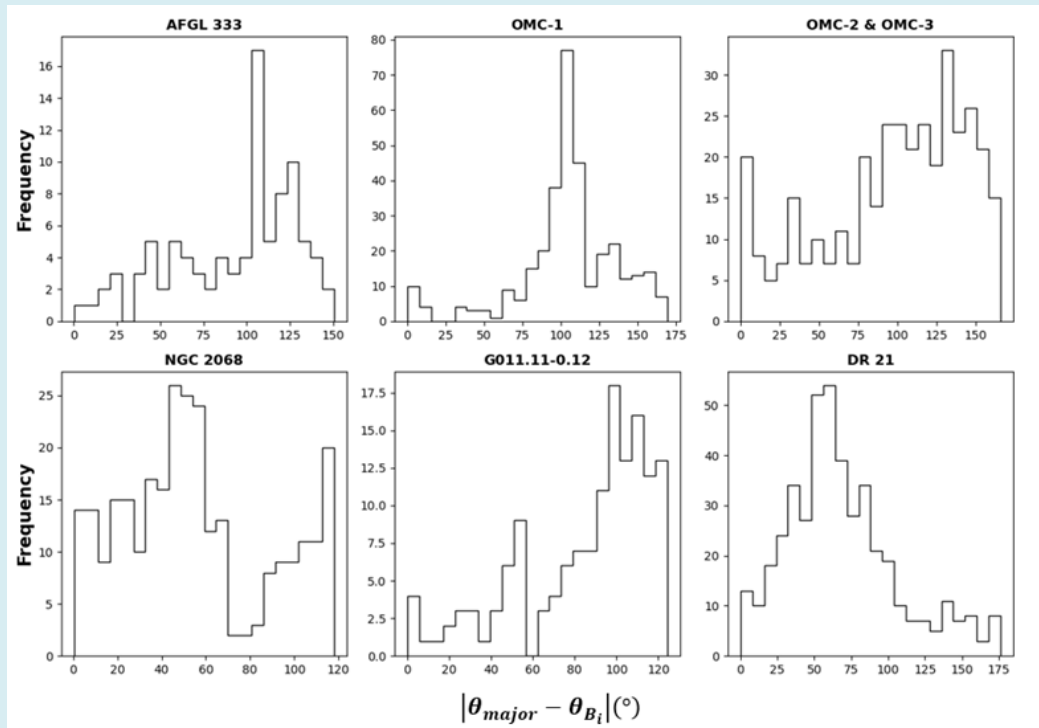
Porel P. Statistical Investigation of B-fields in Cores and Filaments using JCMT/SCUPOL Legacy Survey Archival Data. Open J of Astro 2024, 2(2): 000144.

Copyright© Porel P.

Figure 11: Histogram of the difference between θ_{major} and θ_{Bi} for the filament regions. These histograms show that for all the filament regions the major axis of the filament is almost perpendicular to the observed position angle of the magnetic field (θ_{Bi}).

Discussion

Star Formation in Core Region

In the core region, two distinct categories of particles are present: charged particles, such as electrons and ions, and neutral particles, including atoms and molecules. The dynamics of these particles differ fundamentally due to their interactions with the magnetic field. Charged particles are constrained to traverse along the magnetic field lines, following a helical trajectory, while neutral particles, experiencing no magnetic force, possess the freedom to move in any direction.
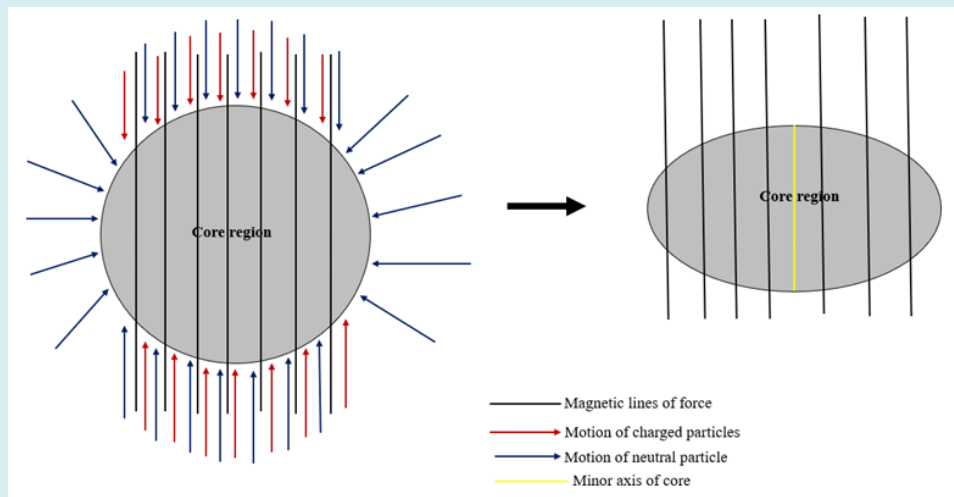

Figure 12: Cartoon model of ambipolar diffusion and contraction of the core region along the magnetic field direction.

As depicted in Figure 12, both charged and neutral particles enter the core region by aligning with the magnetic field lines. However, only the neutral particles can approach the core from various directions.

This results in a greater degree of contraction along the magnetic field lines, causing the minor axis of the core region to align closely with the direction of the magnetic lines of force [55-58]. This phenomenon, known as "ambipolar diffusion", plays a pivotal role in star formation. The extent of contraction along the direction of the magnetic field is contingent upon the degree of ionization; a lower level of ionization leads to a correspondingly diminished contraction.

Through the process of ambipolar diffusion, a core that is initially sub-critical characterized by magnetic energy that surpasses gravitational energy, thus preventing collapse can transition to a super-critical state, where gravitational forces dominate over magnetic influence, allowing for collapse and the potential initiation of star formation. Figure 12 illustrates a cartoon model of ambipolar diffusion, elucidating the alignment of the mean magnetic field direction with the minor axis of the core and demonstrating how the infall of particles within the core region contributes to the onset of star formation.

Star Formation in Filament Region

Filamentary structures typically arise in regions characterized by weaker magnetic fields that are influenced by the surrounding gas flow. Gilberto CG, et al. [59] have demonstrated the U-shaped morphology of the magnetic field in proximity to the filament. In these regions, the gas flows align with the direction of the magnetic field, thereby necessitating that the plane of the sky component of the magnetic field remains perpendicular to the long axis of the filament.

In our investigation, we conducted a comprehensive statistical analysis of the magnetic field morphology within the plane of the sky. Our findings indicate that the orientation of the magnetic field is predominantly parallel to the minor axis of the core region while remaining nearly perpendicular to the major axis of the filament.

Conclusion

- The statistical analysis of the combined polarization measurements in the cores and filaments is summarized as follows:
- The statistical evaluation of the magnetic field morphology within core regions reveals that the plane of the sky component of the mean magnetic field is predominantly parallel to the minor axis of the core regions.
- In several core regions, the outflow direction aligns closely with the large-scale mean magnetic field; however, it exhibits a near perpendicular relationship with the mean magnetic field measured on smaller scales.
- The mean magnetic field direction within core regions demonstrates variability between large and small scales, and this misalignment contributes to a reduction in the degree of polarization (p).
- The analysis of magnetic field morphology in filament regions indicates that the plane of the sky component of the mean magnetic field is largely perpendicular to the major axis of the filament regions.
- In filament regions, the major axis of the filament is almost perpendicular to the observed B-vector position angle values.

Acknowledgements

References

1. Matthews BC, McPhee CA, Fissel LM, Curran RL (2009) The Legacy of SCUPOL: 850 µm Imaging Polarimetry from 1997 to 2005. The Astrophysical Journal Supplement Series 182(1): 143-204.

2. Hull CLH, Plambeck RL, Kwon W, Bower GC, Carpenter JM, et al. (2014) TADPOL: A 1.3 mm Survey of Dust Polarization in Star-forming Cores and Regions 213(1): 13.

3. Liu J, Zhang Q, Qiu K (2022) Magnetic field properties in star formation: A review of their analysis methods and interpretation. Frontiers in Astronomy and Space Sciences 9: 943556.

4. Li HB, Goodman A, Sridharan TK, Houde M, Zhi-Yun Li, et al. (2014) The link between magnetic fields and cloud/star formation. Protostars and planets, pp: 101-123.

5. Shu FH, Adams FC, Lizano S (1987) Star formation in molecular clouds: observation and theory. 25: 23-81.

Porel P. Statistical Investigation of B-fields in Cores and Filaments using JCMT/SCUPOL Legacy Survey Archival Data. Open J of Astro 2024, 2(2): 000144.

Copyright© Porel P.

6. McKee CF, Zweibel EG, Goodman AA, Heiles C (1993) Magnetic Fields in Star-Forming Regions Theory. In: Levy EH, Lunine JI (Eds.), Protostars and Planets 3: 327.

7. Hall JS (1949) Observations of the Polarized Light from Stars. Science 109(2825): 166-167.

8. Hiltner WA (1949) On the Presence of Polarization in the Continuous Radiation of Stars. SAO/NASA Astrophysics Data System (ADS) 109: 471.

9. Hiltner WA (1949) Polarization of Light from Distant Stars by Interstellar Medium. Science 109(2825): 165.

10. Hough JH, Aitken DK, Whittet DCB, Adamson AJ, Chrysostomou A (2008) Grain alignment in dense interstellar environments: spectropolarimetry of the 4.67-μm CO-ice feature in the field star Elias 16 (Taurus dark cloud). Monthly Notices of the Royal Astronomical Society 387(2): 797-802.

11. Lazarian A, Hoang T (2007) Radiative torques: analytical model and basic properties. Monthly Notices of the Royal Astronomical Society 378(3): 910-946.

12. Dolginov Z, Mitrofanov IG (1976) Orientation of Cosmic Dust Grains. Astrophysics and Space Science 43(2): 291-317.

13. Draine T, Joseph C, Weingartner (1996) Radiative Torques on Interstellar Grains. I. Superthermal Spin-up. Astrophysical Journal 470: 551.

14. Andersson G, Lazarian A, Vaillancourt JE (2015) Interstellar Dust Grain Alignment. Annual Review of Astronomy and Astrophysics 53: 501-539.

15. Heiles C (2000) Stars: An Agglomeration of Stellar Polarization Catalogs. The Astronomical Journal 119(2): 923-927.

16. Mestel L, Spitzer L (1956) Star formation in magnetic dust clouds. Monthly Notices of the Royal Astronomical Society 116(5): 503-514.

17. Fiedler RA, Mouschovias TC (1993) Ambipolar Diffusion and Star Formation: Formation and Contraction of Axisymmetric Cloud Cores. II. Results. Astrophysical Journal 415: 680.

18. Tassis K, Dowell CD, Hildebrand RH, Kirby L, Vaillancourt JE (2009) Statistical Assessment of Shapes and Magnetic Field Orientations in Molecular Clouds through Polarization Observations. Monthly Notices of the Royal Astronomical Society 399(4): 1681-1693.

19. Masson J, Chabrier G, Hennebelle P, Vaytet N, Commercon B (2016) Ambipolar diffusion in lowmass star formation: I. General comparison with the ideal magnetohydrodynamic case. Astronomy & Astrophysics 587: 20.

20. (2005) Magnetic Fields in the Universe: From Laboratory and Stars to Primordial Structures. American Institute of Physics Conference Series, 784.

21. Lea~o MRM, de Gouveia Dal Pino EM, Santos-Lima R, Lazarian A (2013) The Collapse of Turbulent Cores and Reconnection Diffusion 777(1): 46.

22. Xu Y, Reid MJ, Zheng XW, Menten KM (2006) The distance to the perseus spiral arm in the milky way. Science 311(5757): 54-57.

23. Enoch ML, Young KE, Glenn J, Evans NJ, Golwala S, et al. (2006) Bolocam survey for 1.1 mm dust continuum emission in the c2d legacy clouds. I. perseus. The Astrophysical Journal 638(1): 293.

24. de Zeeuw PT, Hoogerwerf R, de Bruijne HJ, Brown AGA, Blaauw A (1999) A hipparcos census of the nearby OB associations. The Astronomical Journal 117(1): 354.

25. Ungerechts H, Thaddeus P (1987) A CO survey of the dark nebulae in Perseus, Taurus, and Auriga. Astrophysical Journal Supplement Series 63: 645-660.

26. Kenyon SJ, Dobrzycka D, Hartmann L (1987) A new optical extinction law and distance estimate for the taurus-auriga molecular cloud. The Astronomical Journal 108(5): 1872-1880.

27. Anthony-Twarog JB (1982) The h-beta distance scale for b stars-the orion association. Astronomical Journal 87: 1213-1222.

28. Snell RL, Dickman RL, Huang YL (1990) Molecular outflows associated with a flux-limited sample of bright far-infrared sources. Astrophysical Journal 352: 139-148.

29. Racine R, Van Den Bergh S (1970) Reflection nebulae and spiral structure. In: Symposium International Astronomical Union, Cambridge University Press, USA, 38: 219-221.

30. Walker MF (1956) Studies of Extremely Young CLUSTERS.I.NGC 2264. Astrophysical Journal Supplement 2: 365.

31. Brand J, Blitz L (1993) The velocity field of the outer galaxy. Astronomy and Astrophysics 275: 67-90.

32. Ward-Thompson D, Motte F, Andre P (1999) The initial

conditions of isolated star formation—iii. millimetre continuum mapping of prestellar cores. Monthly Notices of the Royal Astronomical Society 305(1): 143-150.

33. Mamajek EE (2008) On the distance to the ophiuchus star-forming region. Astronomische Nachrichten 329(1): 10.

34. Neckel TH (1978) UBV, VRI and H-beta observations of stars in the H II regions NGC 6334 and NGC 6357. Astronomy and Astrophysics 69: 51-56.

35. Rodriguez LF, Moran JM, Ho PTP, Gottlieb EW (1980) Radio observations of water vapor, hydroxyl, silicon monoxide, ammonia, carbon monoxide, and compact h ii regions in the vicinities of suspected herbig-haro objects. Astrophysical Journal 235: 845-865.

36. Kastner JH, Weintraub DA, Aspin C (1992) The juggler-a three-lobed near-infrared reflection nebula toward crl 2136= oh 17.6+ 0.2. Astrophysical Journal 389: 357-368.

37. De Lara E, Lopez-Molina G, Chavarria KC (1991) Distance to the serpens cloud. II. Astronomy and Astrophysics 243(1): 139-142.

38. Webster AS, Ryle M (1976) Some extended observations of the radio source cl4. Monthly Notices of the Royal Astronomical Society 175(1): 95-104.

39. Carey SJ, Feldman PA, Redman RO, Egan MP, MacLeod JM, et al. (2000) Submillimeter observations of midcourse space experiment galactic infrared-dark clouds. The Astrophysical Journal 543(2): L157-L161.

40. Sridharan TK, Beuther H, Saito M, Wyrowski F, Schilke P (2005) High-mass starless cores. The Astrophysical Journal 634(1): L57.

41. Vallee JP, MacLeod JM (1990) Co spectroscopy of the w48 molecular cloud near 1.3 millimeters. Astrophysical Journal, Part 1 (ISSN 0004-637X) 358: 183-188.

42. HG Marraco and AE Rydgren (1981) On the distance and membership of the R crA T association. Astronomical Journal 86: 62-68.

43. Gwinn CR, Moran JM, Reid MJ (1992) Distance and kinematics of the w49n h2o maser outflow. Astrophysical Journal, Part 1 (ISSN 0004637X) 393(1): 149-164.

44. Genzel R, Downes D, Schneps MH, Reid MJ, Moran JM, et al. (1981) Proper motions and distances of h2o maser sources. ii-w51 main. Astrophysical Journal Part 1 247: 1039-1051.

45. Wilking BA, Mundy LG, Blackwell JH, Howe JE (1989) A millimeter-wave spectral-line and continuum survey of cold iras sources. Astrophysical Journal, Part 1 (ISSN 0004-637X) 345: 257-264.

46. Wendker HJ, Baars JWM (1974) Radio detection of a compact h n-region associated with far-infrared and molecular line emission in cygnus. Astronomy and Astrophysics 33:157.

47. Little LT, Bergman P, Cunningham CT, Heaton BD, Knee LBG, et al. (1988) Iras 20188+ 3928-a molecular cloud with a very dense bipolar outflow. Astronomy and Astrophysics (ISSN 0004-6361) 205: 129-134.

48. Staude HJ, Lenzen R, Dyck HM, Schmidt GD (1982) The bipolar nebula s106photometric, polarimetric, and spectropolarimetric observations. Astrophysical Journal, Part 1 255: 95-102.

49. Preibisch TH, Smith MD (2002) The outflow activity of the protostars in s140 irs. Astronomy & Astrophysics 383(2): 540-547.

50. Wu Y, Zhang Q, Chen H, Yang C, Wei Y, et al. (2005) Co j= 2-1 maps of bipolar outflows in massive star-forming regions. The Astronomical Journal 129(1): 330.

51. Blaauw A, Hiltner WA, Johnson HL (1959) Photoelectric photometry of the association iii cephei. Astrophysical Journal 130(69): 130:69.

52. Soam A, Maheswar G, Chang WL, Sami D, Bhatt HC, et al. (2015) Magnetic field structure around cores with very low luminosity objects. Astronomy & Astrophysics 573: A34.

53. Wouterloot JGA, Brand J, Fiegle K (1993) IRAS sources beyond the solar circle. iii-observations of h_2o, oh, ch_3oh and co. Astronomy and Astrophysics Supplement Series 98(3): 589-636.

54. Leo B, Michel F, Antony SA (1982) Catalog of co radial velocities toward galactic h ii regions. Astrophysical Journal Supplement Series 49: 183-206.

55. Yancy L Shirley, Neal JE II, Kaisa EY, Claudia K, et al. / (2003) A cs j= 5→ 4 mapping survey toward high-mass star-forming cores associated with water masers. The Astrophysical Journal Supplement Series 149(2): 375.

56. Menten KM, Reid MJ, Forbrich J, Brunthaler A (2007) The distance to the orion nebula. Astronomy & Astrophysics 474(2): 515-520.

57. Murray FC, William FH, Harley AT, David N, Richard N, et al. (1982) Far-infrared sources in cygnus x-an extended emission complex at dr 21 and unresolved sources at

Porel P. Statistical Investigation of B-fields in Cores and Filaments using JCMT/SCUPOL Legacy Survey Archival Data. Open J of Astro 2024, 2(2): 000144.

Copyright© Porel P.

s106 and on 2. Astrophysical Journal 261: 550-557.

58. Michael DS (2004) The origin of stars. World Scientific.

59. Gilberto CG, Enrique VS, Manuel ZA (2018) The magnetic field structure in molecular cloud filaments. Monthly Notices of the Royal Astronomical Society 480(3): 2939-2944.

60. Robitaille T, Bressert E (2012) Aplpy: astronomical plotting library in python. Astrophysics Source Code Library, 1208.

61. Ginsburg A, Sipocz MB, Brasseur CE, Cowperthwaite PS, Craig MW, et al. (2019) Astroquery: an astronomical web-querying package in python. The Astronomical Journal 157(3): 98.

62. Green GM (2018) Dustmaps: A python interface for maps of interstellar dust. Journal of Open Source Software 3(26): 695.

Porel P. Statistical Investigation of B-fields in Cores and Filaments using JCMT/SCUPOL Legacy Survey Archival Data. Open J of Astro 2024, 2(2): 000144.

Copyright© Porel P.